# Interaction between gas channels in water-saturated sands

Germán Varas [1], Gabriel Ramos [2,3] and Valérie Vidal [4]

[1] *Instituto de Fisica, Pontificia Universidad Católica de Valparaiso (PUCV), Avenida Universidad 330, Valparaiso, Chile*

[2] *Institut de Mécanique des Fluides (IMFT), CNRS and Université de Toulouse, 31400 Toulouse, France*

[3] *Laboratoire de Génie Chimique (LGC), Université de Toulouse, CNRS, INPT, UPS, 31062 Toulouse, France*

[4] *Laboratoire de Physique, École Normale Supérieure de Lyon, Université de Lyon—CNRS, 46 Allée d'Italie, 69364 Lyon Cedex 7, France*

(Received 6 December 2023; accepted 15 July 2024; published 12 August 2024)

This work investigates the interaction between gas channels in a vertical Hele-Shaw cell when air is injected simultaneously from two points at a constant flow rate. Unlike single-injection experiments, this dual-point system induces the formation of numerous bubbles, thereby intensifying the interactions between air channels. We use an image analysis technique for tracking motion in the granular bed to define a *flow density* parameter throughout the cell. The vertical accumulation of this parameter ($n_z$) reveals two specific heights, one marking a finger-to-fracture transition and another indicating the average interaction height of the air channels. Conversely, its horizontal accumulation ($n_x$) assesses the extent of overlap in the fluidized zones created by each airflow. Notably, the analysis indicates that the optimum distribution of the three phases in the system is more closely related to the interaction's variability than its intensity. This finding is significant for industrial applications such as air sparging and catalytic reactors.

DOI: 10.1103/PhysRevE.110.024901

## I. INTRODUCTION

Multiphase flows through unconsolidated, deformable porous media are encountered in many natural or industrial applications. Among the most striking examples in nature are volcanic eruptions, which may be directly driven by the complex interplay between bubbles and crystals in magma [1,2]. At an even larger scale, massive methane or $CO_2$ emissions at the seafloor were pointed out as responsible for past climate changes [3–5] and are among the most important scientific challenges for hazard prediction [6]. They also play a crucial role in human activities, as subsea gas release triggered by offshore oil and gas production is at the origin of the most deadly incidents [7]. In addition to these risk assessment challenges, such multiphase flows are also involved in soil decontamination by air sparging [8–10] or in three-phase catalytic reactors [11]. In these latter applications, the larger the surface contact area among the three phases (gas/liquid/solid), the more efficient the process, and since decades, the estimation of the so-called gas and liquid holdup in these systems has been attempted, as well as the optimization of the three phases distribution [11,12].

These systems exhibit complex dynamics as capillary, viscous, buoyant, and frictional forces can be at stake together [13]. The complex interplay between these forces may lead to the emergence of patterns [14,15], and the observation of different flow regimes such as percolation, fluidization or fracture of the granular medium [16]. Although some approaches have considered a uniform gas injection and the transition to hydraulic failure and fluidization [17], the amount of literature on localized injection has grown in the last decades due to its importance in the applications mentioned above. We focus here on studies relevant to this work, i.e., localized gas injection at the bottom of an immersed granular medium, in which gravity and buoyancy forces play a fundamental role, being the main force driving the gas rise in the system. In such configuration, different flow regimes are observed from percolation to fluidization, fracture, or even instabilities in the air-channel migration [18–25]. At long times, the repetitive gas rise through the immersed granular layer leads to the formation of a fluidized zone of parabolic shape due to a slow particle convective motion [16,20,21,26–29]. Although recent works have focused on the migration and trapping of bubbles [25,30], little attention has been given to the fundamental study of interacting sources. However, this process is of primary importance in the industrial or natural context as two or more localized sources may coexist and, if close enough, interact. This work focuses on the interaction of two neighboring sources of localized air injection at the bottom of an immersed granular medium. First, we present the experimental setup, first observations, and image analysis (Sec. II). In the next section, we quantify the transient regime (Sec. III A), the air-channel dynamics in the two fluidized zones generated above each injection point as well as their interaction (Sec. III B), and the global dynamics of the interacting fluidized zones (Sec. III C). The fundamental contribution of this work is to quantify four key variables, namely the stabilization time, two specific heights associated with the channel dynamics and interaction, and a proxy for grain motion in the fluidized area. Section III demonstrates that, although all four arise from the interaction between the fluidized zones generated by the two injection points, they display quite different dependence on the flow rate. We finally conclude in Sec. IV, and replace our results in a more general perspective to point out their importance in terms of applications.

 

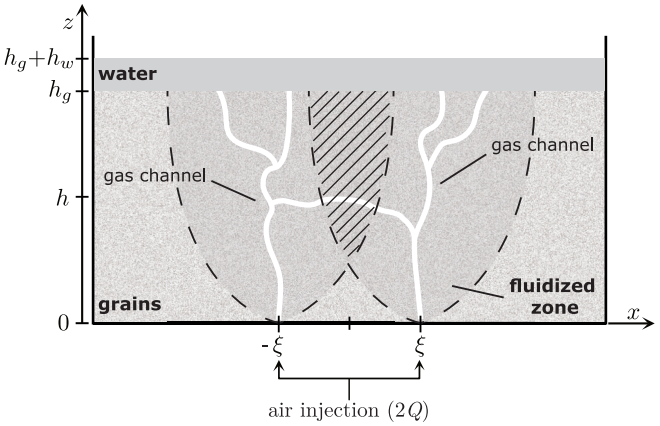


FIG. 1. Sketch of the experimental setup. Air is injected simultaneously at a constant flow rate ($2Q$) at the base of water-saturated sand through two injection nozzles. Each air injection point generates a fluidized zone (dashed lines) in the stationary regime. In a given range of parameters, the air channels rising in the fluidized zones interact in a specific area (hatched region).

## II. METHODS

### A. Experimental setup

The experiment consists of a Hele-Shaw cell (height 50 cm, width 80 cm, gap between the two glass plates 2 mm) filled with a granular layer (height $h_g = 35$ cm) immersed in water (Fig. 1). The water height above the granular bed is $h_w \approx 2$ cm, sufficiently small to prevent grain advection in the water layer and potential crater formation [31]. The grains are polydisperse spherical glass beads (Sovitec glass spheres 250–425) with a diameter $d = 318 \pm 44$ μm from size distribution and a density $\rho_g = 2300$ kg m$^{-3}$. The grains are immersed in water, with a density $\rho_w = 1000$ kg m$^{-3}$. Air is injected at a constant flow rate through two nozzles (inner diameter $d_i \simeq 1$ mm) located at horizontal positions $-\xi$ and $+\xi$ at the cell bottom (Fig. 1). We ensure a constant flow rate $Q$ at each injection point using a mass-flow controller (M+W Instruments, model D-6321) connected to the nozzles via capillary tubes so that any pressure drop associated with gas emission through one nozzle does not affect the flow at the neighboring nozzle. The flow rate $Q$ ranges from 0.66 to 18.26 mL/s. Above this value, a hydraulic fracture occurs, corresponding to the overcoming of the tensile strength of the medium [32] and resulting in a fracture-like behavior of the air rising straight from bottom to top, preventing interaction. The distance between the air injection points is $2\xi \simeq 14$ cm and has been chosen so that both fluidized zones overlap, i.e., $2\xi < 2\sqrt{Dh_g} \simeq 24$ cm, where $D \simeq 4$ cm is the coefficient characterizing the fluidized zone parabolic shape over a single-injection point in our experiment [23]. It should be noted that in the first few millimeters, the channel may undergo small displacements, forming a virtual injection point beside the physical injection point (see Sec. III C). The system dynamics is recorded by a PixeLINK camera (PL-B741U model) capturing one image every 10 s ($\Delta t = 10$ s) with a $1280 \times 800$ px$^2$ resolution, giving an average spatial resolution of about 0.5 mm/px.

### B. First observations

Previous works have highlighted the formation of a fluidized zone of parabolic shape when air is injected locally at the bottom of an immersed granular, as displayed in Fig. 2, left [28,29]. In this system, an upward movement of air, focalized at the fluidized zone center, coexists with a convective movement of the grains, which rise in the central zone and move downwards on the sides [16] (see Supplemental Movie 1 [33]). In the stationary regime, few bubbles are trapped in the fluidized region. Indeed, the convective motion forces them toward the bottom center, where they coalesce with the central air channel, with bubble lifetime exhibiting significant variations depending on their distance to the fluidized zone boundaries [30].

The system looks drastically different in the case of two injection points (Fig. 2, second panel). We report first an overlap of the fluidized zones generated by each gas point and, second, and most notably, a large number of bubbles trapped in the fluidized region. Both air channels are influenced by surrounding trapped bubbles and exhibit an erratic motion above a given height, as well as intermittent horizontal interactions (Fig. 2, second panel), which will be discussed in Sec. III B. This leads to a substantial accumulation of bubbles in the overall fluidized region, facilitating further a spontaneous connection between the air channels and disrupting the fluidized zone's convective movement, which cannot entrain the bubbles back in the gas channels anymore (see Supplemental Movie 2 [33]).

### C. Image analysis

We use a stacking technique of image differences to enhance resolution for detecting air or grain motion within the cell. A brief overview of this method is provided below, and the full description can be found in Refs. [23,29]. The technique calculates the *flow density*, $\rho_n(x, z)$, as the sum of consecutive image differences, $\mathrm{M}_k = |\mathrm{I}_{k+1} - \mathrm{I}_k|$, where $I_k$ is the intensity matrix for image $k$:

$$\rho_n(x, z) = \sum_{k=1}^{n-1} \mathrm{M}_k = \sum_{k=1}^{n-1} |\mathrm{I}_{k+1} - \mathrm{I}_k|. \tag{1}$$

The normalized flow density, $\overline{\rho} = \rho_n / \max(\rho_n)$, quantifies motion in the granular bed from gas or grain movement. Note that the water layer above the grains is excluded from this computation. An example of a flow density map is shown in Fig. 2 (third panel), highlighting the motion density around the gas channels and the overlapping contours of the fluidized zones. We define the horizontal and vertical accumulations, $n_x$ and $n_z$, as the cumulative values of the flow density matrix along the vertical and horizontal axes, respectively:

$$n_x(x, t) = \sum_z \rho_n(x, z) \;\; ; \;\; n_z(z, t) = \sum_x \rho_n(x, z). \tag{2}$$

and their normalized value $\bar{n}_x$ and $\bar{n}_z$ over a given time series. The normalized vertical cumulation, $\bar{n}_z(z)$, is shown in Fig. 2 (right). It displays two local maxima, which we define as the average interaction height $\langle h_I \rangle$ of the gas channels and the finger-to-fracture transition $h^*$ (see Sec. III B). Finally, to observe the dynamics of the system, we define a sliding average over $M = 10$ images ($\bar{n}^M_{x,z}$).

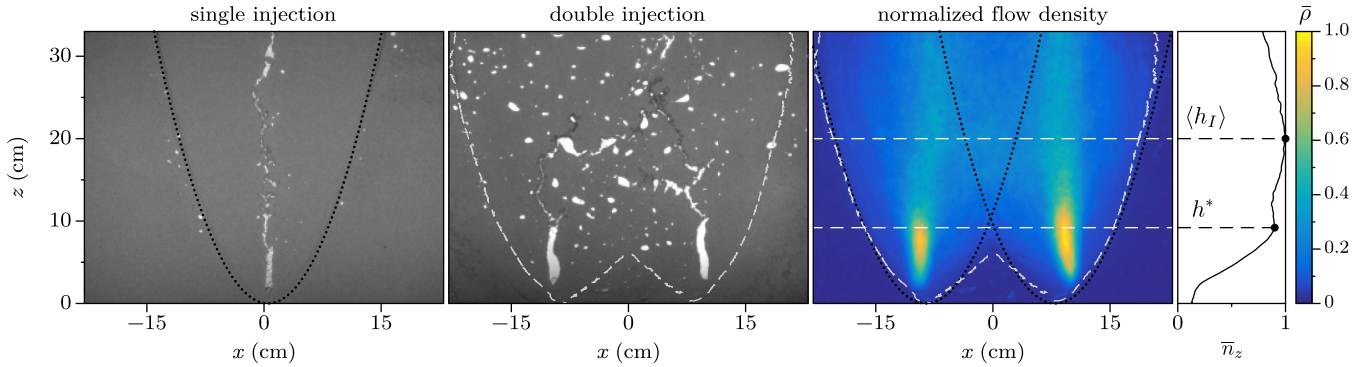


FIG. 2. (Left) Single-injection point ($Q = 2$ mL/s, see Supplemental Movie 1 [33]). The successive passage of air channels creates a fluidized zone of parabolic shape, underlined by the black tracers corresponding to finer grains [16,34]. The black dotted line corresponds to the parabolic contour of the central fluidized zone. (Second panel) Double injection point ($Q = 3.32$ mL/s, see Supplemental Movie 2 [33]). Note the larger number of bubbles compared to a single-injection point and the horizontal channel interaction. (Third panel) Normalized flow density $\overline{\rho}$ for the double injection experiment [stacking over 4000 images, $\Delta t = 10$ s between successive images, corresponding colormap on the right]. (Right) Normalized vertical accumulation $\overline{n}_z$ as a function of $z$. The two local maxima correspond to the average interaction height, $\langle h_I \rangle$, and the finger-to-fracture transition height $h^*$. The black dotted lines indicate the parabolic contours associated with each injection point, based on the outer fluidized zone borders.

## III. RESULTS

In this section, we first describe the transient regime and quantify the stabilization time of the channel (Sec. III A). We then focus on the air-channel dynamics, with a thorough description of its fingering to fracturing transition and the interaction between the two gas channels (Sec. III B). We finally quantify the global dynamics, namely the characteristics of the overall fluidized zone and the interaction region (Sec. III C).

### A. Transient regime

At short times, when the gas first invades the immersed granular medium, it tends to explore a large area in the cell. At the low flow rates in our experiments, the first invasion is mainly through a percolation process, although fluidization may occur locally. The air, therefore, first reaches the free surface at multiple points due to the scattering of the gas arrival at the granular free surface. From this moment on, similarly to the single-injection experiment [29], the development of the final fluidized zone starts at the surface and then spreads downwards. The different air channels rising through the system gradually merge until only two remain. This evolution can be clearly seen when representing the spatiotemporal evolution of the horizontal accumulation $n_x(x, t)$ [Fig. 3(a), top panel]. The stabilization of both channels happens at a time $\tau_s$, hereafter named the stabilization time [white line, Fig. 3(a)]. Although the movement focuses roughly on the vertical of the two injection points, it is distributed almost homogeneously along the vertical axis. Indeed, the spatiotemporal evolution of the vertical accumulation $n_z(z, t)$ [Fig. 3(a), bottom panel] displays, for $t > \tau_s$, a roughly homogeneous background motion (green color), over which are superimposed yellow patches representing the signature of interacting channels.

Figure 4 displays the stabilization time, $\tau_s$, as a function of the airflow rate, $Q$. As expected, the stabilization time decreases drastically when the injection flow rate is increased. It shows a power-law dependence, $\tau_s \propto 1/Q^2$ (Fig. 4, inset). This dependence is consistent with what was previously reported in Ref. [29], although other works had reported a stabilization time-varying as $1/Q$ [35]. Note that a simple argument based on the exploration of a porous matrix predicts accurately that $\tau_s \propto 1/Q^2$ (see details in Ref. [29]).

### B. Air-channel dynamics

The gas rising in the fluidized granular medium experiences a complex dynamics. Above the injection nozzles, it forms a finger rising through the medium, which stops then fractures the above immersed granular layer (Sec. III B 1). Then, we also report a peculiar interaction between the two air rises, contributing to bubble generation in the fluidized region (Sec. III B 2).

#### *1. Finger-to-fracture transition*

In the stationary regime, the air rises above each injection point as a vertical finger. The surrounding medium thus acts as an effective fluid. Similarly to what was already reported in the case of a single gas injection point at the bottom of an immersed granular material, this finger propagates upwards and then stops. Beyond this point, due to the continuous air injection, the gas fractures the medium [23,36]. This transition can be clearly seen in Fig. 2, second panel. As it happens at an almost constant height $h^*$ for a given flow rate, it is associated with a maximum in $\bar{n}_z$ (first maximum from the bottom in the example shown in Fig. 2, right panel). Note that it does not always correspond to the first maximum (see Sec. III B 2), but it can be easily identified as it is always associated with the maxima in the flow density matrix (yellow spots, Fig. 2, third panel). Figure 5 (open symbols) displays the evolution of $h^*$ as a function of the gas flow rate $Q$. Similarly to previous experimental results for a single gas channel, $h^*$ increases linearly with $Q$ [36]. This linearity can be retrieved by the simple following argument. Let us consider the generalized Darcy law, which gives the finger rising velocity $v = v(t)$ and

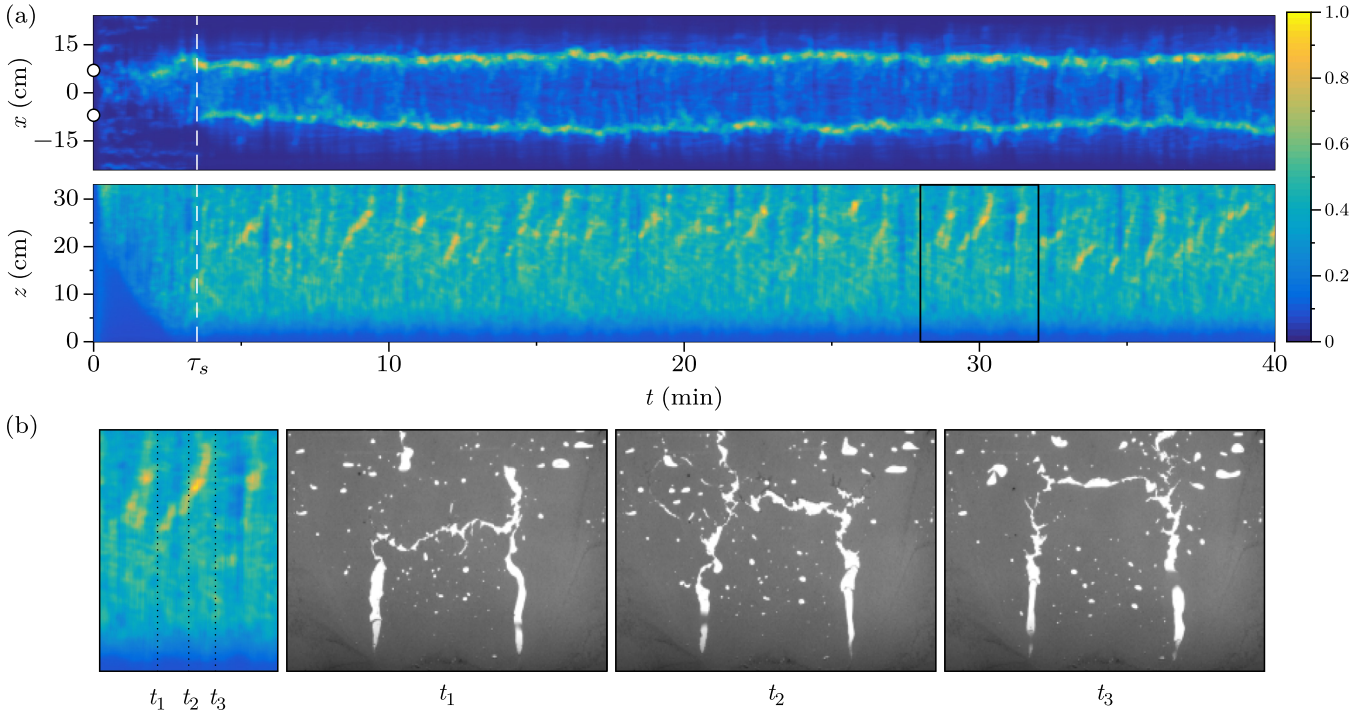


FIG. 3. (a) Spatiotemporal diagram of $\bar{n}_x^M$ (top panel) and $\bar{n}_z^M$ (bottom panel) ($Q = 6.64$ mL/s). The stabilization time $\tau_s$ is indicated by the white dashed line (here $\tau_s \simeq 4$ min) and corresponds to the stabilization of the two main air channels. The movement focuses roughly on the vertical of the two injection nozzles indicated by the white dots (top panel) while it is almost homogeneously distributed along the vertical axis (bottom panel). Sporadic unions between both channels are occasionally observed (bottom panel, yellow lines). (b) Tracking the connection between the two air channels. (Left) Zoom corresponding to the black rectangle in panel (a), focusing on the channels interaction. (Second to last panels) Pictures at three successive times show the evolution of the horizontal interaction between the two air channels. As seen in the spatiotemporal diagram, this connection rises through the system and is frequently repeated throughout the experiment.

accounts for the buoyancy forces:

$$v = \alpha\left(\frac{P_{\text{top}} - P_0}{h_g - h} - \rho g\right), \tag{3}$$

with $\alpha = e^2/12\eta$, $e$ the cell gap, and $(\eta, \rho)$ the effective viscosity and density of the particle-laden fluid, respectively. $P_{\text{top}}$ is the pressure in the upper part of the finger, $P_0$ the atmospheric pressure (neglecting here the water height above the granular layer), $h_g$ the initial granular layer height (Fig. 1), $h$ the finger height at time $t$ and $g = 9.81$ m s$^{-2}$ the gravitational acceleration.

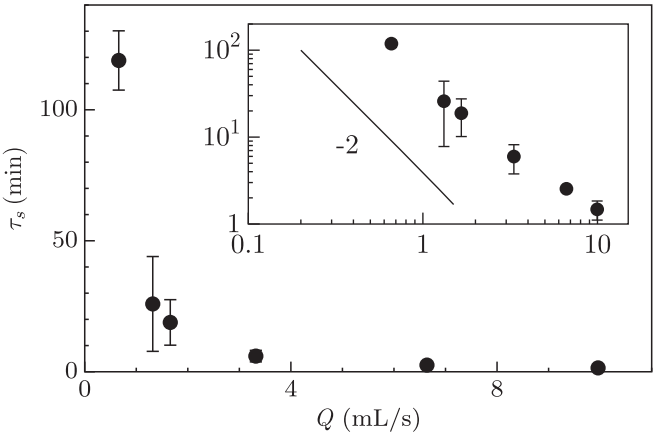


FIG. 4. (a) Stabilization time of the air channels $\tau_s$ as a function of the flow rate $Q$. The time is computed as the duration for the last channel to stabilize. Inset: The data follow a power law, $\tau_s \propto 1/Q^2$.

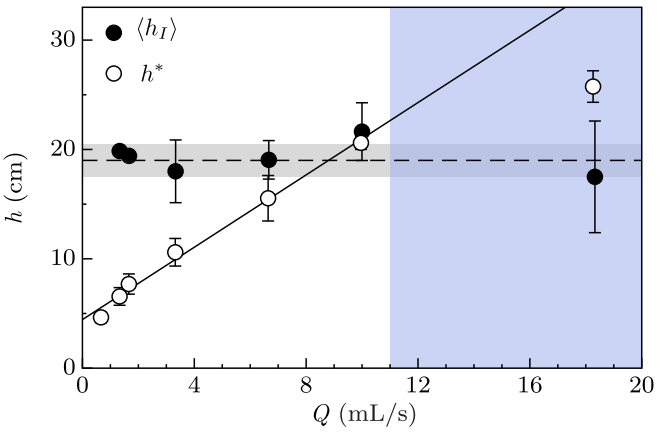


FIG. 5. Finger-to-fracture transition $h^*$ (white dots) and average air-channel interaction height, $\langle h_I \rangle$ (black dots) as a function of the gas flow rate $Q$. The solid line shows the linear behavior of $h^*$ with $Q$. The blue region indicates the region in which $h^* \simeq \langle h_I \rangle$ and departs from its linear behavior. The dashed line represents the average interaction height across all flow rates, and the gray region indicates the standard deviation.

The effective density of the medium above the gas channel is $\rho = \phi\rho_g + (1-\phi)\rho_w \simeq 1730$ kg m$^{-3}$, where $\phi \simeq 56\%$ is the loose random packing fraction in the fluidized zone. The effective viscosity is estimated using the semiempirical model of Zarraga *et al.* [37], which quantifies the viscosity of dense suspensions for packing fractions up to 60%,

$$\eta = \eta_w \frac{e^{-2.34\phi}}{(1-\phi/\phi_m)^3}, \tag{4}$$

where $\phi_m = 62\%$ corresponds to the maximum poured random packing, leading to $\eta \simeq 0.3$ Pa s.

Assuming a Poiseuille flow of the gas in the finger, the flow rate can be written as

$$Q = \beta\left(\frac{P_{\text{down}} - P_{\text{top}}}{h}\right), \tag{5}$$

with $P_{\text{down}}$ the pressure at the injection point, $\beta = we^3/12\eta_{\text{air}}$, $w$ the finger width and $\eta_{\text{air}} = 1.8 \times 10^{-5}$ Pa s the air dynamic viscosity. Experimentally, the finger width $w$ remains roughly constant, of about $w \simeq 1$ cm. The pressure at the injection point can be estimated as $P_{\text{down}} = P_0 + \rho g h_g + 4\gamma/d_i$ where $\gamma = 72$ mN/m is the air-water surface tension and $d_i$ the inner nozzle diameter (see Sec. II A).

Combining the previous equations makes it possible to link the finger rise velocity $v$ to its height $h$ as

$$v = \frac{\alpha}{h_g - h}\left(\rho g h + \frac{4\gamma}{d_i} - \frac{hQ}{\beta}\right). \tag{6}$$

The finger-to-fracture transition may then be defined as follows. The granular medium will fracture when the finger velocity $v$ becomes larger than the grain rearrangement velocity $v_s$. This latter velocity is typically of the order of magnitude of the Stokes velocity, $v_s \sim d^2\Delta\rho g/18\eta_w$, with $\Delta\rho = \rho_g - \rho_w$ the density difference between the particles and fluid. The finger will then compact quickly the above grain layer and stop. The pressure inside will, therefore, rise up to the critical point until it is able to fracture the above granular layer up to the surface. Considering $Q/\beta \ll (v_s/\alpha + \rho g)$, which is always true in our experimental range, gives the finger-to-fracture transition height:

$$h^* \simeq \frac{(v_s/\alpha)h_g - 4\gamma/d_i}{v_s/\alpha + \rho g}\left(\frac{Q}{(v_s/\alpha + \rho g)\beta} + 1\right). \tag{7}$$

We therefore retrieve a linear variation of $h^*$ with $Q$. Figure 6(a) compares the experimental data with the prediction given by Eq. (7). For $\phi \simeq 56\%$ (loose random packing fraction), the model predicts $h^* \simeq 27$ cm for $Q = 10$ mL/s [dark orange curve, Fig. 6(a)], to be compared with the experimental value of $h^* = 20.6 \pm 0.6$ cm. This approximate model therefore succeeds in predicting the order of magnitude of $h^*$. However, although it predicts a linear variation of $h^*$ with $Q$, as reported in the experiments, it fails to predict the correct slope when varying $Q$. Indeed, for a fixed packing fraction $\phi$, $h^*$ predicted by the model does not vary significantly in the range $Q = [0-20]$ mL/s. However, the packing fraction influences strongly the finger-to-fracture transition height $h^*$ [colored lines, Fig. 6(a)]. In addition, Fig. 6(a) reports the model prediction for a fixed grain diameter, $d = 318$ μm, while the solid particles are polydisperse and exhibit a large

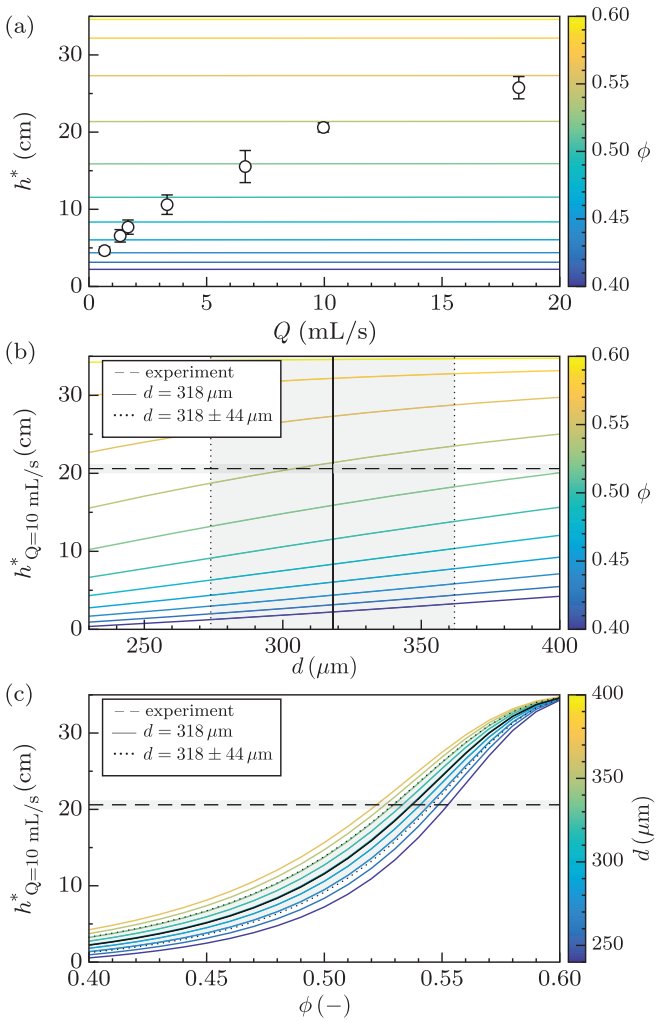


FIG. 6. (a) Comparison between the experimental values of the finger-to-fracture transition height $h^*$ (white dots, same than Fig. 5) and the model [Eq. (7) with $d = 318$ μm]. The colorbar indicates different values of the packing fraction $\phi$. (b, c) Model prediction of $h^*$ for a fixed flow rate (here $Q = 10$ mL/s), as a function of (b) the particle diameter $d$, for different values of $\phi$ (colorbar and colored lines) and (c) the packing fraction $\phi$, for different values of $d$ (colorbar and colored lines). The experimental value is reported as the horizontal black dashed line, with its standard deviation corresponding to the surrounding light gray region. The solid and dotted lines in panels (b) and (c) indicate the average grain diameter ($d = 318$ μm, solid black line) and its variation estimated from the polydisperse size distribution ($d = 318 \pm 44$ μm, dotted black lines).

distribution ($d = 318 \pm 44$ μm). To explore further the dependence of the model prediction on the parameters $d$ and $\phi$, we estimate with Eq. (7) the finger-to-fracture transition height $h^*$ for a fixed flow rate, here $Q = 10$ mL/s. Figure 6(b) displays $h^*_{Q=10\text{ mL/s}}$ as a function of the particle diameter $d$, for different values of $\phi$ (colorbar and colored lines). The experimental value is reported as the horizontal black dashed line, with its standard deviation corresponding to the surrounding light gray region. The vertical solid and dotted lines indicate the average grain diameter and its variation estimated from the polydisperse size distribution, $d = 318 \pm 44$ μm. Figure 6(c) shows

the evolution of $h^*_{Q=10\ \mathrm{mL/s}}$ when varying the packing fraction $\phi$, for different particle diameter (colorbar and colored lines). The black lines and light gray region indicate the same as in Fig. 6(b).

Although simplistic, the above model not only provides the correct order of magnitude for the finger-to-fracture transition height, but also points out the influence of the different parameters. In particular, it highlights the drastic impact of the packing fraction $\phi$ on $h^*$. The model relies on simple assumptions and does not account for the complex interplay that may exist between the flow-rate and the local packing fraction at the tip of the air finger. The grain diameter affects less the variations of $h^*$. However, grains polydispersity is not accounted for by the model, and could have further impact on the finger-to-fracture height estimation. Note that in both the model and experiments, $h^*$ does not tend to zero when $Q \to 0$. This is due to the fact that at very small $Q$, the air only percolates through the grain matrix and does not fluidize the granular layer anymore, therefore prohibiting any gas finger formation. The model is then not valid anymore. Conversely, at high $Q$, $h^*$ departs from the linear trends (blue region, Fig. 5). This behavior will be discussed in the next section.

#### 2. Gas channels interaction

Above the finger-to-fracture transition height, a peculiar phenomenon is reported. The two gas channels interact by forming a horizontal fracture, first right above $h^*$, then repetitively up to a given height [see Fig. 3(b), picture at $t_1$, for example]. This dynamics repeats in time and displays a clear pattern on the spatiotemporal diagram representing $\bar{n}^M_z(z,t)$ [Fig. 3(a), bottom panel, and Fig. 3(b)]. It is associated with a maximum in $\bar{n}_z$ (second maximum from the bottom in the example shown in Fig. 2, right panel). This maximum makes it possible to define an average interaction height, $\langle h_I \rangle$. Interestingly, this average gas channel interaction height remains constant when varying the flow rate $Q$ (Fig. 5, black dots) and, for high flow rates, becomes smaller than $h^*$.

In this fracturing regime, the physical arguments developed in the above Sec. III B 1 do not hold, as the immersed grains cannot be considered an effective fluid anymore. However, the order of magnitude of $\langle h_I \rangle$ can be retrieved by considering the simple following argument. To propagate by fracturing, the air in the channel has to overcome the pore overpressure, given by $\Delta P \simeq \gamma/\epsilon d$, where $(\epsilon d)$ is the typical pore size in the grain pile, with $\epsilon$ of the order of a few percents. The gas channel will preferentially lift the above layer rather than open a path through the grains when its tip reaches the height $h_c$ such that $\rho g h_c = \Delta P$, where $\rho$ is the effective density of the medium (see Sec. III B 1). We thus get the critical height $h_c = \gamma/\rho g \epsilon d$. Taking $\epsilon \simeq 5$–$7\%$ leads to $h_c \simeq 18$–$26$ cm, of the order of the average interaction height. We can, therefore, interpret $\langle h_I \rangle$ as the height at which a channel starts lifting the above water-grains layer and exploring the horizontal direction – leading to an interaction with the neighboring channel in the case the fluidized zones overlap.

### C. Global dynamics

In this section, we quantify the global dynamics of the system, namely the properties of the overall fluidized zone. First, we use the horizontal cumulation to quantify the movement resulting, in particular, from the interaction between the two fluidized regions generated by each injection point (Sec. III C). Second, we compute the theoretical interaction area between two fluidized zones of parabolic shape, discuss the discrepancy with the observed overall fluidized region, and propose a proxy to quantify the real interaction area (Sec. III C 2).

#### 1. Horizontal cumulation

An important point for many applications is how the solid-liquid phases (grains-water) or all three phases are distributed in the system and how these phases interact with each other in time. From the flow density computation, we represent in Fig. 7(a) the horizontal cumulation, $\bar{n}_x(x)$. It displays two maxima, representative of the strong motion of the air channels at the vertical of the injection nozzles. The fact that the central value, $\bar{n}_x(0)$, is not null is the signature of the fluidized zones overlapping. A theoretical estimation of $\bar{n}_x(x)$ can be obtained as follows. We consider that the overall fluidized zone corresponds to the simple addition of two single source contributions located at $x = \pm\xi$. Following Ramos *et al.* [29], we write the horizontal cumulation for each source as the sum of the contribution of a central air channel, taken as a Gaussian (amplitude $a$, standard deviation $\sigma$) and of a spatially homogeneous region (constant amplitude $c$) limited by a parabola, $z = (x \pm \xi)^2/D$:

$$n_x^{\mathrm{single}}(x) = \int_{\frac{(x\pm\xi)^2}{D}}^{h_g} c\, dz + \int_0^{h_g} a\, e^{-\frac{(x\pm\xi)^2}{2\sigma^2}}\, dz. \tag{8}$$

Note that $D$ can be interpreted as a diffusion coefficient or rather, having the dimension of a length, a diffusive length. For a single source located at $x = \pm\xi$, integrating both terms in Eq. (8) and normalizing leads to

$$\bar{n}_x^{\mathrm{single}}(x) = (1-A) - \frac{(x\pm\xi)^2}{D'} + A \exp\left(-\frac{(x\pm\xi)^2}{2\sigma^2}\right), \tag{9}$$

with $A = a/(c+a)$ and $D' = D h_g (c+a)/c$ (see Eq. (11) in Ref. [29]). Adding the two contributions in $x = \pm\xi$ therefore gives the following expression for two sources separated by a distance $2\xi$:

$$\bar{n}_x(x) = 2(1-A) - \frac{2}{D'}(x^2+\xi^2) + 2A \cosh\left(\frac{\xi x}{\sigma^2}\right) \times \exp\left(-\frac{x^2+\xi^2}{2\sigma^2}\right). \tag{10}$$

The horizontal cumulation $\bar{n}_x(x)$ depends on four parameters, namely $\xi$, $\sigma$, $A$, and $D$. The source location coordinate $\xi$ is fixed experimentally ($\xi = 14$ cm). The standard deviation of the Gaussian contribution $\sigma$ corresponds roughly to the width of the air finger, which is experimentally measured and found to be equal for either one or two injection points, $\sigma \simeq 1$ cm. The two remaining unknown parameters, $A$ and $D'$, are directly linked to $a$ and $c$, the amplitudes of the Gaussian central air-channel contribution and of the homogeneous region, respectively.

The solid line in Fig. 7(a) represents the best adjustment of the experimental data with Eq. (10) with two free parameters

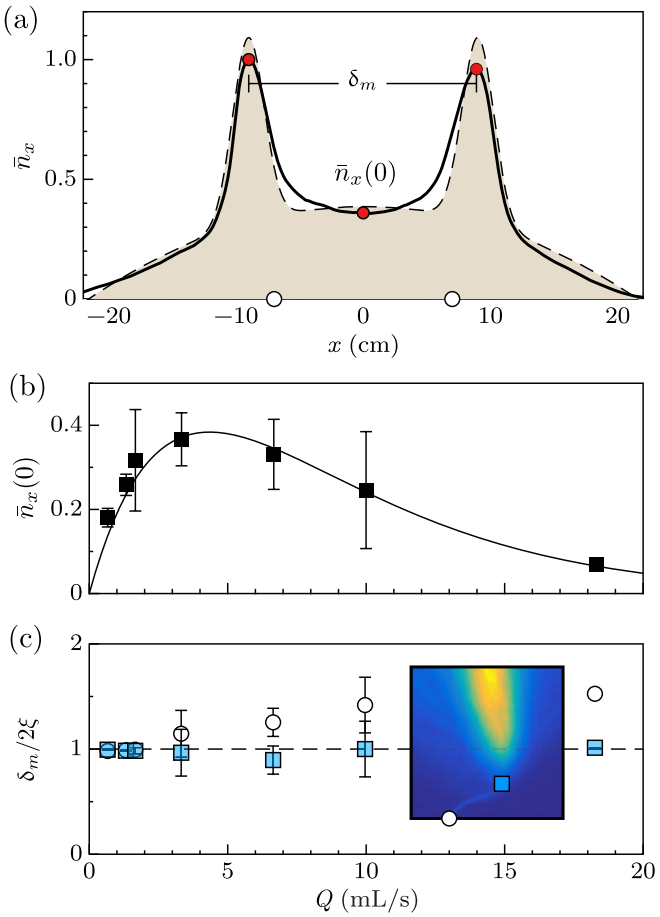


FIG. 7. (a) Normalized horizontal cumulation, $\bar{n}_x$, as a function of $x$ ($Q = 6.67$ mL/s). We note $\bar{n}_x(0)$, the minimum value of $n_x$ at the center of the cell, and $\delta_m$, the distance between the two local maxima. The white dots at $\bar{n}_x = 0$ indicate the position of the injection nozzles separated by a distance $2\xi$. The red dots indicate the maxima and the central minimum of the solid black curve, used to quantify $\delta_m$ and $\bar{n}_x(0)$. The results (dashed line) are well-fitted by the superposition of two noninteractive injection points (solid line). (b) $\bar{n}_x(0)$ as a function of the injected flow rate $Q$ (black curve is a guideline). (c) Maximum interaction distance $\delta_m$ normalized by the injection distance ($2\xi$) (open circles) and by the virtual injection points distance (light blue square). Inset: Zoom on the flow density map close to the injection nozzle at $x = +\xi$ (Fig. 2, third panel) showing the injection point (open circle) and the virtual injection point (light blue square).

to match the constants in the model. We recover the main shape of $\bar{n}_x$ with the two maxima and the central value of $\bar{n}_x(0)$, although the model does not adjust the exact curve shape in the central region. Indeed, instead of a local minimum as predicted by Eq. (10), $\bar{n}_x$ displays a Totoro shape [38]. This highlights the fact that the overall fluidized zone cannot be considered simply as the sum of two fluidized regions, as will be commented further in Sec. III C 2.

Figure 7(b) displays the value of $\bar{n}_x(0)$ as a function of the flow rate $Q$ injected at each source. This parameter provides a good estimation of the grains motion at the center of the cell ($x = 0$). The curve is nonmonotonous and exhibits a maximum, at a flow rate $Q_{\max} \simeq 3$ mL/s. Contrary to intuition, the most effective grain motion in the overlapping zone is not for the highest flow rates but for intermediate ones. Two possible explanations can be proposed. First, when the flow rate increases, the air explores the system more and more and has a tendency to generate more bubbles and more movement in the granular layer, leading to an increase in $\bar{n}_x(0)$. However, for higher flow rates, the air channels tend to be more focalized and rise more straightforward, which could be at the origin of the decrease of $\bar{n}_x(0)$ for $Q > Q_{\max}$. A second explanation is the following. We observe in Fig. 7(a) that the distance between the two maxima of the Totoro shape, $\delta_m$, is slightly larger than $2\xi$. Figure 7(c) (white dots) displays the variations of $\delta_m/(2\xi)$ as a function of $Q$. Although it remains equal to 1, as expected, for low flow rates, we observe that for $Q > Q_{\max}$, it increases for increasing $Q$. Figure 7(c) inset shows a zoom on the flow density map close to the injection point at $x = +\xi$. Although the air is injected at a given location, the system forms a small gas channel, the top end of which acts as a virtual source for the associated fluidized region. These virtual sources tend to repel each other, and for $Q > Q_{\max}$, their distance increases when $Q$ increases. Rescaling $\delta_m$ by the distance between these virtual sources instead of the imposed $\pm\xi$ makes all the data collapse on the dashed curve representing unity [Fig. 7(c), blue squares]. If the distance between the virtual sources increases, then the interaction area between the two fluidized zones generated by each source should decrease, which may explain the decrease in $\bar{n}_x(0)$ observed for $Q > Q_{\max}$, and its nonmonotonous variation as a function of $Q$.

#### 2. Interaction area

The interaction area $A_I$ between two parabolas limited to a height $h_g$ is represented by the hatched zone in Fig. 1. Defining the two parabolas as $z = (x \pm \xi)^2/D$, it can be obtained by simple geometrical analysis:

$$A_I = \frac{4}{3}\sqrt{D}h_g^{3/2} + \frac{2}{3}\frac{\xi^3}{D} - 2h_g\xi\,. \tag{11}$$

Note that this relationship is valid only if $\sqrt{Dh_g} > \xi$; below this value, the parabolas do not overlap and $A_I = 0$. The interaction area depends on the coefficient $D$, the height $h_g$, and the distance between the origins (injection points in our experiments) $2\xi$.

Figure 8(a) presents the parametric study of $A_I$ as a function of $D$ for different $\xi$. The interaction area is null for $D \leqslant D_c = \xi^2/h_g$, the critical coefficient under which the parabolas do not intersect [Fig. 8(a), dots]. For $D > D_c$, the curves exhibit a monotonic growth, and the slope at small $A_I$ is primarily determined by the proximity of the injection points ($\xi$). The bold line in Fig. 8(a) represents the curve for our experimental parameters. Determining $D$ in our system is not an easy task. As shown in Sec. III C 1, the overall fluidized zone cannot be described simply as the superposition of two parabolas generated by each source. Indeed, we clearly see in Fig. 2, third panel, that the inner branches of the supposed parabolas have a larger diffusion coefficient than the outer branches. Determining $D$ from the inner or outer contours proved to be challenging. Indeed, contrary to the fluidized zone borders of a single source, it is not possible to fit a parabola from bottom to top in either case. A rough estimation

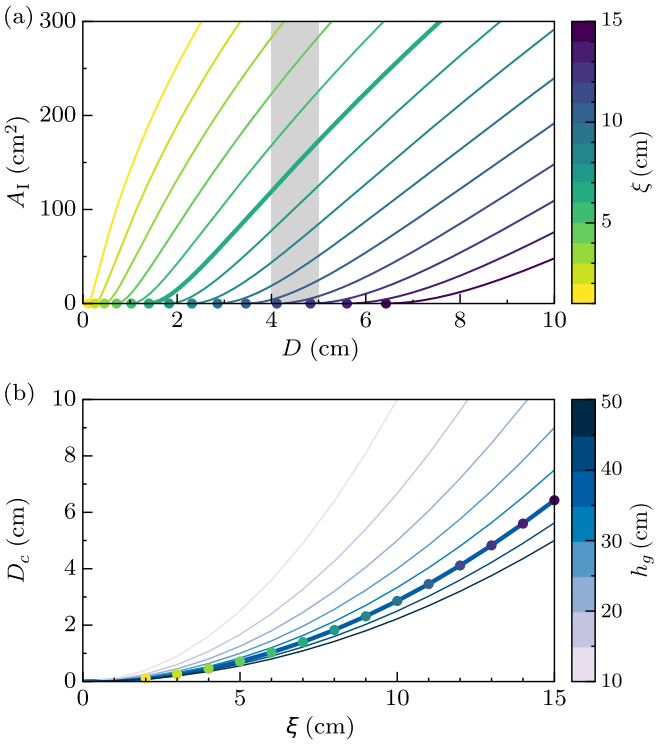


FIG. 8. (a) Interaction area as a function of the coefficient $D$ for different distances between the source $2\xi$ the colormap indicates the value of $\xi$. The bold line corresponds to $\xi = 7$ cm, and the vertical gray zone defines the values for $D = [4–5]$ cm (see text). The dots for $A_I = 0$ indicate the critical coefficient below which $A_I = 0$ for each $\xi$. (b) Critical coefficient $D_c$ as a function of $\xi$ for different granular layer heights $h_g$. The bold line corresponds to our experimental value ($h_g = 35$ cm). The colored dots are the critical $D_c$ reported from (a).

gives $D = [4–5]$ cm whichever $Q$, Reporting this range in Fig. 8(a) (gray region) provides an estimation of the interaction area, $A_I \simeq 145 \pm 35$ cm$^2$. A good proxy to estimate the interaction area would be $A_I^m = \delta_m(h_g - \langle h_I \rangle)$, which can be easily determined from $\bar{n}_x(x)$ and $\bar{n}_z(z)$. Such estimation for our experiments leads to $A_I^m \simeq 225$ cm$^2$. Although they are of the same order of magnitude, these values cannot be directly compared, as $A_I^m$ is, by definition, expected to be larger than $A_I$. Further experiments varying $\xi$ would be required to check the robustness of this proxy.

Figure 8(b) displays the variation of the critical coefficient $D_c$ as a function of $\xi$ for different granular layer heights $h_g$. The bold line stands for our experiments. If varying (and estimating) $D$ proves to be difficult in our experiments, variations of $\xi$, once again, may prove useful to see how the interaction area, when varying, affects the system dynamics and the overall fluidized zone geometry.

## IV. CONCLUSION

This work presents an experimental study of gas injection into water-saturated sands with two interacting sources. The results demonstrate that going from a single to two injection points significantly increases the number of bubbles trapped in the overall fluidized zone, resulting in a complex interaction between the air channels. This observation highlights how the configuration of the injection points impacts the dynamics of the three-phase system, a key aspect for enhancing our understanding of these processes (see Sec. I).

Analyzing the accumulation of movement along the vertical ($\bar{n}_z$) uncovers two local maxima, contrasting with previous studies that reported only one maximum [29]. The first maximum, situated directly above the injection points, corresponds to a finger-to-fracture transition. The proposed model accurately predicts the critical height $h^*$ for both channels, although it fails to predict its dependence on the flow rate. The second maximum, emerging above the finger-fracture transition, only exists when considering multiple injection points. This is attributed to the lateral interactions between air channels, modifying the vertical rise expected for a single-injection point only. Based on a simplified model, we interpret the associated height $h_I$ as the height at which the air channel starts to lift the grain-water layer, thereby exploring the horizontal direction and interacting with the adjacent channel.

We analyzed the horizontal movement distribution ($\bar{n}_x$) to quantify the interaction between the air channels. The results display two local maxima indicative of the air channels' motion and a central zone, distinct from zero, confirming the channel interaction. They are well-fitted by considering two superimposed, noninteracting point sources. Interestingly, the movement in the central zone exhibits an optimum at an intermediate flow rate ($Q \simeq 3$ mL/s). It can be interpreted as a competition between the generation of more bubbles when the flow rate increases and the air channels' focalization at high flow rates, which reduces the gas exploration. Moreover, past a critical flow, the air exhibits a thin, localized channeling close to the injection points, generating virtual gas sources slightly repelling each other and widening the effective distance between them. Finally, we computed the total interaction area using two parabolic equations based on the grain layer height $h_g$, coefficient $D$, and the source distance $2\xi$. This method yields an analytical result comparable to the experimental estimate. However, the robustness of this proxy would require varying the distance between the sources to be checked.

The take-home message of this work is that the four key variables, namely $\tau_s$, $h^*$, $\langle h_I \rangle$, and $\bar{n}_x(0)$, which all four arise from the interaction between the fluidized zones generated by two injection points, display quite different dependence on the flow rate. The stabilization time $\tau_s$ of the air channels exhibits an inverse quadratic dependence on the airflow, a similar dependence to what has been previously demonstrated for a single-injection point [29]. It seems, therefore, that the stabilization time is not affected by the number of air channels. The finger-to-fracture transition $h^*$ increases linearly with the flow rate, whereas the height at which the air channels begin an horizontal exploration, $\langle h_I \rangle$, remains roughly constant. Both dependencies can be accounted for by simple models. Finally, $\bar{n}_x(0)$ represents the movement at the midpoint between the injection points and reveals a complex dependence with the flow. No overall model, at present, is able to account for the connection between these four variables, and their dependence with the flow rate.

This work paves the way for future research on how multiple injection points coexist and interact in complex ways, highlighting the need for further studies. Unanswered

questions remain, such as the impact of the injection points distance on bubble generation and how this parameter might significantly influence the bubble production efficiency, which is crucial in industrial applications. Future exploration should, therefore, consider the extension from two to several injection points up to a uniform, continuous gas injection. We expect in particular an increasing complexity in the sources interaction, with a direct impact on the gas holdup which is a crucial parameter, for instance, in heterogeneous catalysis. Last, the interaction of air channels offers a chance to quantify their dynamics using statistical analysis or techniques like particle image velocimetry, promising valuable insights into the dynamics within the fluidized zone.

## ACKNOWLEDGMENTS

G.V. and V.V. acknowledge financial support from FONDECYT Project No. 11121300. This work was supported by the Programa de cooperación científica ECOS/CONICYT Grant No. C14E07. G.V. and V.V. thank the Centre National de la Recherche Scientifique (CNRS) for providing support for this collaboration.

[1] J. Oppenheimer, A. C. Rust, K. V. Cashman, and B. Sandnes, Front. Phys. **3**, 60 (2015).
[2] S. Vergniolle and N. Métrich, Bull. Volcanol. **84**, 83 (2022).
[3] H. Svensen, S. Planke, A. M.-S. Renssen, B. Jamtveit, R. Myklebust, T. R. Eidem, and S. S. Rey, Nature (London) **429**, 542 (2004).
[4] F. May, M. Warsitzka, and N. Kukowski, Int. J. Greenhouse Gas Control **90**, 102805 (2019).
[5] M. Foschi, J. A. Cartwright, C. W. MacMinn, and G. Etiope, Proc. Natl. Acad. Sci. USA **117**, 27869 (2020).
[6] V. Vidal and A. Gay, Pap. Phys. **14**, 140011 (2022).
[7] J. E. Olsen and P. Skjetne, Can. J. Chem. Eng. **94**, 209 (2016).
[8] W. Ji, A. Dahmani, D. P. Ahlfeld, J. D. Lin, and E. Hill III, Ground Water Monit. Rem. **13**, 115 (1993).
[9] K. R. Reddy, S. Kosgi, and J. Zhou, Hazard. Waste Hazard. Mater. **12**, 97 (1995).
[10] M. C. Brooks, W. R. Wise, and M. D. Annable, Ground Water Monit. Rem. **19**, 105 (1999).
[11] G. Biardi and G. Baldi, Catal. Today **52**, 223 (1999).
[12] R. C. Darton and D. Harrison, Chem. Eng. Sci. **30**, 581 (1975).
[13] R. Juanes, Y. Meng, and B. K. Primkulov, Phys. Rev. Fluids **5**, 110516 (2020).
[14] B. Sandnes, H. A. Knudsen, K. J. Måløy, and E. G. Flekkøy, Phys. Rev. Lett. **99**, 038001 (2007).
[15] B. Sandnes, E. G. Flekkøy, H. A. Knudsen, K. J. Måløy, and H. See, Nat. Commun. **2**, 288 (2011).
[16] G. Varas, J.-C. Géminard, and V. Vidal, Granular Matter **15**, 801 (2013).
[17] T. Mörz, E. A. Karlik, S. Kreiter, and A. Kopf, Sediment. Geol. **196**, 251 (2007).
[18] H. Geistlinger, G. Krauss, D. Lazik, and L. Luckner, Water Resour. Res. **42**, W07403 (2006).
[19] M. Stöhr and A. Khalili, Phys. Rev. E **73**, 036301 (2006).
[20] J. S. Selker, M. Niemet, N. G. McDuffie, S. M. Gorelick, and J.-Y. Parlange, Transp. Porous Med. **68**, 107 (2007).
[21] X.-Z. Kong, W. Kinzelbach, and F. Stauffer, Chem. Eng. Sci. **64**, 1528 (2009).
[22] R. Mourgues, D. Bureau, L. Bodet, A. Gay, and J. B. Gressier, Earth Planet. Sci. Lett. **313-314**, 67 (2012).
[23] G. Varas, G. Ramos, J.-C. Géminard, and V. Vidal, Front. Phys. **3**, 44 (2015).
[24] Z. Sun and J. C. Santamarina, J. Geophys. Res.: Solid Earth **124**, 2274 (2019).
[25] S. Lee, J. Lee, R. Le Mestre, F. Xu, and C. W. MacMinn, Phys. Rev. Fluids **5**, 084307 (2020).
[26] R. Semer, J. A. Adams, and K. R. Reddy, Geotech. Geol. Eng. **16**, 59 (1998).
[27] X.-Z. Kong, W. Kinzelbach, and F. Stauffer, Chem. Eng. Sci. **65**, 4652 (2010).
[28] G. Varas, V. Vidal, and J.-C. Géminard, Phys. Rev. E **83**, 011302 (2011).
[29] G. Ramos, G. Varas, J.-C. Géminard, and V. Vidal, Phys. Rev. E **92**, 062210 (2015).
[30] R. Poryles, V. Vidal, and G. Varas, Phys. Rev. E **93**, 032904 (2016).
[31] G. Varas, V. Vidal, and J.-C. Géminard, Phys. Rev. E **79**, 021301 (2009).
[32] E. Detournay, Annu. Rev. Fluid Mech. **48**, 311 (2016).
[33] See Supplemental Material at http://link.aps.org/supplemental/10.1103/PhysRevE.110.024901 for the system dynamics produced by one and two injection points.
[34] G. Varas, V. Vidal, and J.-C. Géminard, Phys. Rev. E **83**, 061302 (2011).
[35] P. Philippe and M. Badiane, Phys. Rev. E **87**, 042206 (2013).
[36] V. De Zotti and V. Vidal, in *Compte-rendus de la 17e Rencontre du Non-Linéaire*, edited by E. Falcon, M. Lefranc, F. Pétrélis, and C. T. Pham (Non-Linéaire Publications, Paris, 2014), pp. 29–34.
[37] I. E. Zarraga, D. A. Hill, and D. T. Leighton, J. Rheol. **44**, 185 (2000).
[38] H. Miyazaki, *My Neighbor Totoro* (50th Street Films, New York, NY, 1988).